Journal of Materials Chemistry A

PAPER

View Article Online
View Journal

Cite this: DOI: 10.1039/c7ta00893g

Hybrid n-type $Sn_{1-x}Ta_xO_2$ nanowalls bonded with graphene-like layers as high performance electrocatalysts for flexible energy conversion devices†

Yandong Duan,‡[ab] Nianqing Fu,‡[c] Sibai Li,‡[a] Xiaoyang Yang,[a] Jiaxin Zheng,*[a] Yuan Lin*[ab] and Feng Pan *[a]

Received 26th January 2017
Accepted 9th March 2017

DOI: 10.1039/c7ta00893g

rsc.li/materials-a

We report here hybrid n-type Ta-doped SnO_2 ($Sn_{1-x}Ta_xO_2$) nanowalls (as an electron-rich donor) bonded with graphene-like layers ($Sn_{1-x}Ta_xO_2$/C) as high performance electrocatalysts for flexible energy conversion devices. SnO_2 possesses high electron mobility (125–250 $cm^2\ V^{-1}\ S^{-1}$), and Ta doping is adopted to increase the electron concentration to further improve the conductivity of the SnO_2 film to allow its use as a catalyst support. Our first-principles calculations reveal that the increased electrical conductance is mainly attributed to the increased intrinsic doping effect caused by the substitution of Sn by Ta. The Ta-doped SnO_2 not only acts a well conductive support for the close coated graphene-like carbon layers but also pushes electrons to the carbon electrocatalyst to enhance its catalytic performance. Advanced features of these nanowall films include not only a high specific surface area, and good adhesion to substrates, but also flexibility. One application as a counter electrode in fully flexible dye-sensitized solar cells (DSSCs) shows that the optimal power conversion efficiency (PCE) of fully flexible DSSCs is 8.38% under AM1.5G illumination (100 mW cm^{-2}), which is one of the highest PCEs for fully flexible DSSCs.

Introduction

Electrocatalysts for the oxidation–reduction reaction are crucial in fuel cells,[1–3] water splitting,[4–6] dye-sensitized solar cells (DSSCs),[7–9] and other electrochemical devices. Platinum (Pt) is the most common choice for these electrocatalytic reactions due to its high conductivity, excellent catalytic activity, and chemical stability, but its scarcity and high cost limit its large-scale utilization. Replacing Pt catalysts with cheap and commercially available materials is a key issue in the development of renewable-energy technologies. Recently, intense efforts have been made to explore alternative materials to replace Pt materials, such as carbon materials,[10–12] polymers,[13,14] transition metal compounds and other hybrid materials.[15,16] Among these materials, carbonaceous materials are the most promising substitute due to their wonderful conductivity, excellent catalytic activity, and low cost.

However, carbon materials often suffer from poor adhesion to the substrate, which will result in detachment of carbon from the substrate, leading to disadvantageous effects on device performance and long-term stability.[11,17] For this reason, formation of a high quality carbon film on the substrate is crucial. To overcome this disadvantage, some studies were attempted to add TiO_2 or SnO_2 to improve this bonding strength.[18,19] However, it was found that adding too much TiO_2 can weaken the catalytic activity of the carbon counter electrode due to the low conductivity of TiO_2.[20] The general reaction mechanism of the triiodide reduction can be written as:

$$I_3^-(sol) \leftrightarrow I_2(sol) + I^-(sol)\ fast \quad (1)$$

$$I_2(sol) + 2^* \rightarrow 2I^*\ fast \quad (2)$$

$$I^* + e^- \rightarrow I^-(sol)\ slow \quad (3)$$

where * represents the free site on the catalyst surface and sol indicates the electrolyte solution. Steps (1) and (2) have been verified to be usually fast and step (3) is relatively slow to play as the rate-determining step.[21,22] So the ability to provide electrons has been considered to be a key factor for the catalytic activity.

[a]School of Advanced Materials, Peking University, Peking University Shenzhen Graduate School, Shenzhen 518055, China. E-mail: panfeng@pkusz.edu.cn

[b]Beijing National Laboratory for Molecular Sciences, Key Laboratory of Photochemistry, Institute of Chemistry, Chinese Academy of Sciences, Beijing 100190, China

[c]School of Material Science and Engineering, South China University of Technology, Guangzhou 510640, China

† Electronic supplementary information (ESI) available: Digital photographs of the plastic working electrode; computational details for the Ta doping section; N_2 adsorption–desorption isotherms of $Sn_{0.925}Ta_{0.075}O_2$ and $Sn_{0.925}Ta_{0.075}O_2$/C; specific resistivity of $Sn_{1-x}Ta_xO_2$ nanowall films; configuration of fully flexible dye-sensitized solar cells in this study; *j–V* curves based on $Sn_{1-x}Ta_xO_2$/C hybrid structures; long-term stability of DSSCs; and results of the impedance measurements. See DOI: 10.1039/c7ta00893g

‡ These authors contributed equally to this work.

Table 1 The recently reported high values of η obtained for fully flexible DSSCs (2013–2016)

CEs[a]	WEs[b]	η (%)	η of Pt (%)	References
Transparent Ni–Se alloy	Ti foil/TiO_2	7.35		24
Pt-sputtered ITO/PEN[c]	ITO/PEN/P25/MHAT[d]	—	5.6	25
TiN	ITO/PEN/TiO_2	8.10		26
Pt-sputtered ITO/PET[e]	ITO/PEN/TiO_2 nanotube	—	4.18	27
Pt wire	Ti wire/TiO_2		7.41	28
Graphene fiber	Ti wire/TiO_2	2.14	3.25 (Pt wire)	29
Pt wire	Ti wire/TiO_2	—	4.75	30
CuS network	Ti foil/TiO_2 nanotube	6.38	5.6	31
Pt wire	Ti wire/TiO_2 + Nb_2O_5	—	9.1	32
Pt wire	Ti wire/TiO_2	—	6.6	32
Ti foil/Pt	Ti foil/TiO_2 nanotube	—	9.62	33
Pt/ITO/PET	Ti foil/TiO_2	—	5.05	34
Ni foil/CNT/graphene	ITO/PEN/TiO_2 NPs[f]	3.9	3.4 (Pt on ITO-PEN)	35
Pt-sputtered ITO/PEN	ITO/PEN/mesoporous TiO_2 beads	—	6.67	36
Pt/ITO/PEN	Ti foil/TiO_2 NPs	—	5.67	37
Ti/$Sn_{0.925}Ta_{0.075}O_2$/C	ITO/PEN/TiO_2 NPs	8.38	8.46	Our work

[a] Counter electrodes. [b] Working electrodes. [c] Indium tin oxide-coated polyethylene naphthalate. [d] Mesoporous hierarchical anatase TiO_2. [e] Polyethylene terephthalate. [f] Nanoparticles.

Furthermore, to enhance PCE, the thicknesses of these types of carbon counter electrodes need to be above ten micrometers. Such a thick carbon counter electrode increases the device internal resistance and thus hinders device performance by reducing the fill factor.[23] Additionally, flexible devices are required to have high flexibility with good shape bending for daily use or transportation, therefore the adhesion problem will be more serious. Table 1 shows the reported high values of PCE obtained for fully flexible DSSCs based on TiO_2 photoanodes and various counter electrodes. There is still much room for improvement of the performance of fully flexible DSSCs that can be achieved by developing effective methods.

Here, we designed new hybrid catalysts with the $Sn_{1-x}Ta_xO_2$/C nanostructure with attachment of graphene-like carbon layers onto $Sn_{1-x}Ta_xO_2$ nanowalls. Nanowall arrays of $Sn_{1-x}Ta_xO_2$ were grown on Ti foil, and the Ta doping can increase the electronic conductivity of the film, making it a good support for carbon catalyst materials. These nanowall films also have a high specific surface area, good adhesion to substrates, and flexibility. First principles calculations reveal that Ta-doping not only increases the electronic conductivity of SnO_2 but also reduces the work function of SnO_2 remarkably, which makes the electron transfer from SnO_2 to graphene oxide easy. All these factors make this new $Sn_{1-x}Ta_xO_2$/C system exhibit good stability and electrocatalytic activity for electrochemical reduction. One example for its applications is: when used as a counter electrode in flexible DSSCs, the optimal PCE of DSSCs is 8.38% under AM1.5G illumination (100 mW cm^{-2}), which is close to that of control DSSCs with a platinized counter electrode prepared by pyrolysis (8.46%).

Experimental methods

Materials

$SnCl_4 \cdot 5H_2O$ (98%, Sinopharm Chemical Reagent Co., Ltd), $TaCl_5$ (99.8%, Alfa), glucose (AR, Sinopharm Chemical Reagent Co., Ltd), 3-methoxypropionitrile (MPN, 99%, GC, Alfa), LiI (AR, Acros), I_2 (AR, Acros) and 4-*tert*-butylpyridine (TBP, AR, Aldrich) were commercially available and used without further purification. 3-Hexyl-1-methylimidazolium iodide (HMII) was prepared according to the literature.[38]

Synthesis of $Sn_{1-x}Ta_xO_2$ nanowalls and the carbon coating process

Before growing SnO_2, a Ti foil (0.1 mm thickness) was subjected to treatment in 0.5 M hydrofluoric acid aqueous solution for 2 min and subsequently ultrasonically cleaned in distilled water and acetone, respectively.

The SnO_2 nanowalls were fabricated directly onto Ti foil by dipping into a deposition solution containing 0.3 M $SnCl_4 \cdot 5H_2O$ and 0.8 M thioacetamide in a mixture of ethanol and isopropyl alcohol (v/v = 1/3) in a 15 mL centrifuge tube. The solution was heated to 75 °C in a water bath for 3 h. Then, the substrates were removed and washed with water and ethanol, dried and calcined in air at 500 °C for 1 h. For preparing the Ta-doped samples, $TaCl_5$ was added to ethanol (molar ratios of Ta and Sn were 2.5 : 100, 5 : 100, 7.5 : 100, and 10 : 100) to start the reaction. The obtained samples were denoted as $Sn_{0.975}Ta_{0.025}O_2$, $Sn_{0.95}Ta_{0.05}O_2$, $Sn_{0.925}Ta_{0.075}O_2$, and $Sn_{0.9}Ta_{0.1}O_2$, respectively.

The carbon coating process was realized in two steps. First, the as-prepared $Sn_{1-x}Ta_xO_2$ nanowalls were loaded into a sealed Teflon reactor containing 16 g glucose and 120 mL distilled water. A reaction temperature of 180 °C for 4 h was used. After the reaction was completed, the carbon-coated samples were carefully washed with ethanol and dried in an oven at 100 °C for 4 h. Then, carbonization was achieved in a tube furnace by calcining at 500 °C for 2 h in an Ar/H_2 (v/v = 95/5) atmosphere.

Characterization

The morphology of the nanowall films was characterized by scanning electron microscopy (SEM, S-4800, Hitachi) at an

operating voltage of 10.0 kV. The X-ray diffraction patterns were obtained by using a D/MAX-2500 diffractometer (Rigaku Co.) with Cu Kα radiation ($k = 0.15406$ nm) operated at 40 kV and 150 mA. High resolution transmission electron microscopy (HRTEM) was performed with a Tecnai G2 20 S-TWIN transmission electron microscope operated at 200 kV. X-ray photoelectron spectroscopy analysis was carried out using a VG Scientific Escalab 220i-XL spectrometer with standard Al KR radiation, and the working pressure is $<3 \times 10^{-9}$ mbar. The specific surface area was analyzed by Brunauer–Emmett–Teller (BET) nitrogen adsorption–desorption measurements (Micromeritics, ASAP 2020 HD88). The structure of the carbon layer in the hybrid was identified by Raman spectroscopy (iHR 320, Horiba Jobin Yvon, 532.1 nm Laser).

Synthesis of the TiO_2 photoanode and cell fabrication for flexible DSSCs

TiO_2 photoanodes were prepared according to the literature.[39,40] TiO_2 nanoparticles (P25, Degussa) were subjected to pre-sintering at 450 °C for 30 min to remove the contaminants on the surface. 0.6 g P25 was dispersed in a mixture of anhydrous ethanol and *n*-butanol (v/v = 1 : 1) by ultrasonic dispersion for 1 h. After 12 h magnetic stirring, the suspension formed a uniform TiO_2 colloid (15–20 wt%), and 180 μL SITO-sol (Sb, In-doped SnO_2 sol) was added into the P25 colloid to form a modified TiO_2 paste.[40]

Before film coating, a very thin TiO_2 compact layer was deposited on the well cleaned ITO/PEN substrates from tetra-*n*-butyl titanate (TBT) through spin-coating followed by hydrolysis in distilled water at 100 °C. The TiO_2 paste was coated on the substrates by the doctor-blade technique. A 4–5 μm thick second layer of 300–500 nm sized light scattering rutile particles (the paste containing a certain amount of SITO-sol) was deposited using a doctor blade onto the first layer. The dried films were exposed to UV irradiation (300 W) for 30 min, followed by immersion in 100 °C distilled water for 30 min. The digital photograph of the as-prepared working electrode is shown in Fig. S1.† All films were dried in a 100 °C oven for 1 h before being sensitized in a 0.5 mM N_3 dye/ethanol solution overnight for dye adsorption. The electrolyte was a mixture of LiI (0.5 M), I_2 (0.05 M), TBP (0.6 M) and HMII (0.6 M) in MPN. The reference counter electrode was Pt-coated FTO.

Electrochemical tests

The photocurrent density–voltage (*j*–*V*) measurement was performed using a Keithley 2611 Source Meter (Keithley Instruments, Inc.). The light source was an AM 1.5 solar simulator (91160A, Newport Co.). The incident light intensity was 100 mW cm^{-2} calibrated with a standard Si solar cell. The tested solar cells were masked to a working area of 0.2 cm^2. Cyclic voltammetry (CV) was carried out in an N_2-purged acetonitrile solution of 0.1 M $LiClO_4$, 10 mM LiI, and 1 mM I_2 at a scan rate of 50 mV s^{-1} by using a Solartron SI 1287 electrochemical interface system. Platinum wire served as a counter electrode and the saturated calomel electrode (SCE) was used as a reference electrode. Tafel polarization curves were measured with a Solartron SI 1287 electrochemical interface system in a dummy cell with a scan rate of 10 mV s^{-1}. Electrochemical impedance spectroscopy (EIS) data were obtained under 100 mW cm^{-2} illumination, using a perturbation of ±10 mV over the open-circuit potential by using a Solartron 1255B frequency analyzer and Solartron SI 1287 electrochemical interface system. The specific resistivity was measured using a four-probe technique (KDY-1, Kunde Technology).

Computational details

In order to model the SnO_2 doped by Ta, a $3 \times 3 \times 2$ supercell based on the unit cell was constructed, allowing us to investigate different substitution degrees of $Sn_{1-x}Ta_xO_2$, with x ranging from $x = 0$ to 0.125 in steps of $\Delta x = 0.025$, as shown in Fig. S2.† The *k*-point mesh is set to $3 \times 3 \times 4$. The *k*-point mesh is set to $5 \times 5 \times 8$ to calculate the electronic properties. And we use six layers of SnO_2 to simulate the SnO_2 surface and build a supercell with graphene adsorbed on the SnO_2 surface. SnO_2 in the (110) orientation is chosen because it is observed in the experiment and is stable. To prevent spurious interactions between periodic images, a vacuum buffer space is set with the value of at least 15 Å. The *x* and *y* directions are fixed while the *z* direction can be relaxed during optimizing $Sn_{1-x}Ta_xO_2$/C. For optimizing graphene, graphene oxide and $Sn_{1-x}Ta_xO_2$, *x*, *y* and *z* directions can be relaxed. The Brillouin zone is sampled by $5 \times 5 \times 1$ special *k*-points, using the Monkhorst–Pack scheme.[41] All calculations are performed using the plane-wave projector-augmented wave method[42,43] as implemented in the Vienna *ab initio* simulation package.[44,45] The Perdew–Burke–Ernzerhof (PBE)[46] form of generalized gradient approximation (GGA) is chosen as the exchange-correlation potential. To obtain reliable optimized structures, the maximum residual force is less than 0.01 eV $Å^{-1}$ and the energies are converged to within 5×10^{-6} eV per atom. An energy cut-off of 550 eV is used in all cases.

Because the absolute position of energy levels in a bulk calculation is ill-defined by density functional theory (DFT) calculations, here we pick the deep core levels of a Sn atom (far from the doped Ta atom) to align the energy levels in different calculations.

Results and discussion

Design, preparation, and characterization of the $Sn_{1-x}Ta_xO_2$/C nanostructures

The design ideas of $Sn_{1-x}Ta_xO_2$/C nanostructures can be depicted as following: (1) compared with TiO_2, SnO_2 possesses much higher electron mobility (125–250 $cm^2\ V^{-1}\ S^{-1}$ for SnO_2 *vs.* ~1 $cm^2\ V^{-1}\ S^{-1}$ for TiO_2); (2) introducing n-type doping can increase the electron concentration to further improve the electronic conductivity; (3) as mentioned in the introduction part, carbonaceous materials are a promising substitute for Pt due to their excellent catalytic activity and low cost; (4) $Sn_{1-x}Ta_xO_2$ can serve as a good conductive support for such carbon electrocatalyst materials; (5) SnO_2 nanowall structures not only have large surface areas but also facilitate the close carbon coating and its flexibility.

Fig. 1 presents the design and synthesis strategy of the hybrid $Sn_{1-x}Ta_xO_2$/C nanostructure. Ti foil was selected as the substrate material for the photocathode based on the following considerations: (1) it is a conductive material and can be replaced by Cu foil, stainless steel, or other materials; (2) it is a flexible material; and (3) it can be calcined at high temperatures. Hybrid structures were fabricated by coating $Sn_{1-x}Ta_xO_2$ nanowalls with carbon layers and the digital photographs of the prepared samples are shown in Fig. 2.

Fig. 2(a)–(c) show the digital photographs of Ti foil, $Sn_{0.925}Ta_{0.075}O_2$ grown on Ti foil and $Sn_{0.925}Ta_{0.075}O_2$/C grown on Ti foil. Fig. 2(d) and (e) show field-emission scanning electron microscopy (FESEM) top-surface images of a typical as-synthesized carbon-coated nanowall array sample at both low and high magnification. A highly uniform array of nanowalls is obtained, with an average wall thickness of approximately 50–100 nm, and the spacing between the walls ranges from hundreds of nanometers to one micron. The inset of Fig. 2(d) is a cross-sectional view of the same film with a thickness of approximately 3.3 μm, indicating that the nanowalls adhere to the Ti substrate tightly without buffer layers and the walls are almost vertically aligned. Also, the nanowall film has a high surface-to-volume ratio that helps achieve more surface for carbon coating. The specific surface area calculated with the BET equation was 89.1 $m^2\ g^{-1}$ for $Sn_{0.925}Ta_{0.075}O_2$, and 119.7 $m^2\ g^{-1}$ for $Sn_{0.925}Ta_{0.075}O_2$/C. N_2 adsorption–desorption isotherms of the corresponding samples are shown in Fig. S3.† Fig. 2(f) and (g) show the TEM images of the nanowall scratched from the Ti substrate. From Fig. 2(g), we can observe that the nanowalls are the aggregation of nanoparticles, which is confirmed by the electron diffraction pattern in the inset of Fig. 2(g). The TEM images in Fig. 2(g) and (h) indicate that the external surface of the nanowall was uniformly encapsulated with a 4–8 nm thick layer of carbon. Moreover, the HRTEM image in Fig. 2(h) shows the lattice structure of the nanowall in the sample. We can observe 0.335, 0.264, and 0.176 nm for the lattice spacing between (110), (101), and (211) planes, in good agreement with the strongest (110), (101), and (211) peaks in the above XRD measurements. From the HRTEM image of such a hybrid structure (Fig. 2(i)), we can see clearly the graphene-like carbon layers with several nanometer thickness. The Raman

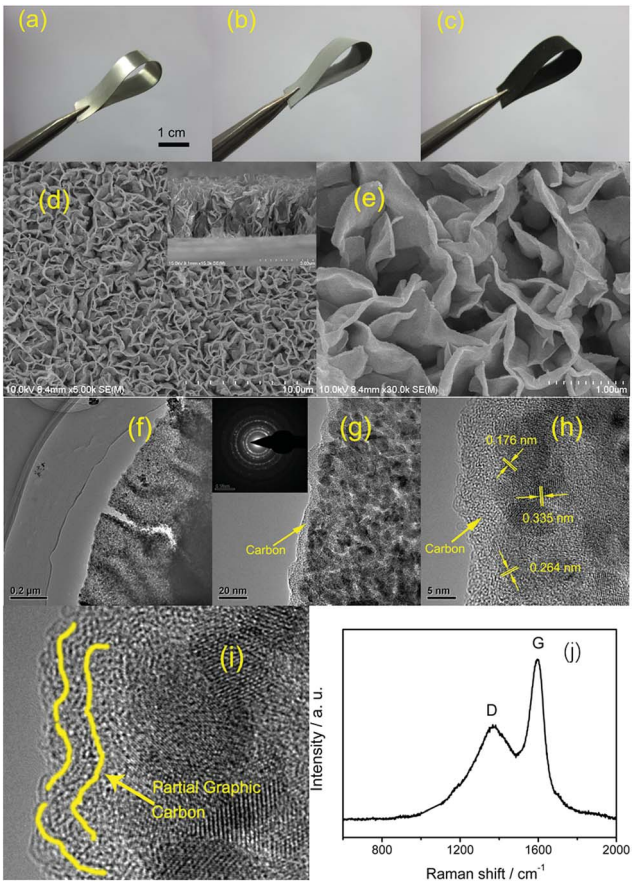

Fig. 2 Digital photographs of (a) Ti foil, (b) $Sn_{0.925}Ta_{0.075}O_2$ grown on Ti foil and (c) $Sn_{0.925}Ta_{0.075}O_2$/C grown on Ti foil. (d) and (e) Top-view SEM images of $Sn_{0.925}Ta_{0.075}O_2$/C grown on the Ti substrate; inset of (d): cross-sectional SEM image of the $Sn_{0.925}Ta_{0.075}O_2$/C sample; (f) and (g) TEM images of $Sn_{0.925}Ta_{0.075}O_2$/C and the corresponding selected area electron diffraction pattern (SAED). (h) High-resolution TEM image of $Sn_{0.925}Ta_{0.075}O_2$/C. (i) High-resolution TEM image of $Sn_{0.925}Ta_{0.075}O_2$/C. (j) The Raman spectrum of $Sn_{0.925}Ta_{0.075}O_2$/C.

spectrum of the $Sn_{0.925}Ta_{0.075}O_2$/C hybrid is shown in Fig. 2(j). There are two characteristic peaks at 1370 and 1596 cm^{-1}, respectively, corresponding to the D band and G band of carbon ($I_G : I_D = 1.7$). The D-band illustrates the defects and disordered portions of carbon, while the G-band stands for the ordered graphitic crystallites of carbon.

Fig. 3(a) shows the X-ray diffraction patterns of the undoped SnO_2, $Sn_{0.925}Ta_{0.075}O_2$, and $Sn_{0.925}Ta_{0.075}O_2$/C samples grown on the Ti substrate. Except for the peaks originating from the Ti substrate, all the diffraction peaks can be indexed to the standard SnO_2 tetragonal rutile type phase, which is consistent with the values in the standard card (JCPDS card no. 88-0287).[47,48] The crystallite size was estimated with the Scherrer equation. From the full width at half maximum of the strongest rutile diffraction (110), the crystallite size was calculated to be *ca.* 12 nm for SnO_2 and $Sn_{0.925}Ta_{0.075}O_2$ samples. No diffraction peaks corresponding to carbon were observed in the XRD pattern of $Sn_{0.925}Ta_{0.075}O_2$/C, meaning that the carbon coating is amorphous.

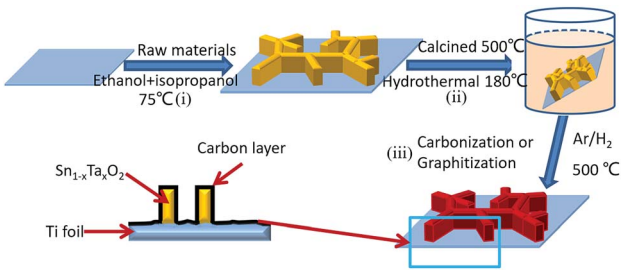

Fig. 1 Schematic flow diagram for the preparation of carbon-layer coated $Sn_{1-x}Ta_xO_2$ nanowalls on Ti foil: (i) $Sn_{1-x}Ta_xO_2$ growth on Ti foil in ethanol and isopropanol solution, (ii) carbon coating process and (iii) carbonization and graphitization processes.

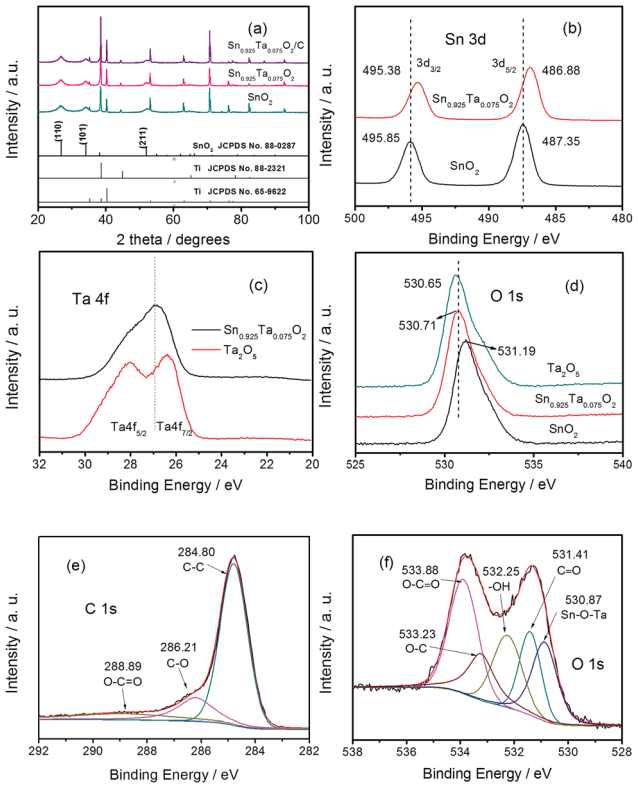

Fig. 3 (a) X-ray diffraction patterns of the samples grown on the Ti substrate. Both undoped SnO_2 and Ta-doped SnO_2 had been calcined at 500 °C for 1 h in air. $Sn_{0.925}Ta_{0.075}O_2$/C: carbon coated $Sn_{0.925}Ta_{0.075}O_2$ sample. (b)–(d) XPS spectra of Sn 3d and Ta 4f for SnO_2 and $Sn_{0.925}Ta_{0.075}O_2$ samples. Ta_2O_5 was used as a reference here. To get clear information about Sn and Ta elements, samples without carbon coating were used here. (e) and (f) XPS spectra of C 1s and O 1s for the $Sn_{0.925}Ta_{0.075}O_2$/C sample.

To analyze the elemental and chemical states of Sn and Ta in our samples, XPS measurements were employed. Fig. 3(b) shows the Sn 3d XPS spectra of the SnO_2 and $Sn_{0.925}Ta_{0.075}O_2$ samples. The two peaks of the Sn 3d spectra of the $Sn_{0.925}Ta_{0.075}O_2$ show a slight negative shift compared with that of SnO_2, which is likely attributed to the interaction between tin atoms, oxygen atoms, and tantalum atoms. Consistent with this result, the Ta 4f spectrum of $Sn_{0.925}Ta_{0.075}O_2$ reveals a positive shift toward higher binding energy compared to those of SnO_2 (Fig. 3(c)). This can be attributed to the variation in electronegativities of the Sn and Ta elements (Sn = 1.96, Ta = 1.5). These observations confirm the formation of the Sn–O–Ta structure in the Ta-doped SnO_2, owing to the substitution of Sn by Ta. In the $Sn_{0.925}Ta_{0.075}O_2$ sample (Fig. 3(d)), the binding energy of the lattice oxygen is located at 530.71 eV, which is between 530.65 eV (Ta_2O_5) and 531.19 eV (SnO_2), owing to the variation in electronegativities of the two metal elements.

As depicted in Fig. 3(e), $Sn_{0.925}Ta_{0.075}O_2$/C shows three distinctive C 1s binding energies, 284.8 eV for non-oxygenated C, 286.21 eV for carbon in C–O, and 289.2 eV for carboxylate carbon (O–C=O), respectively.[49–51] The percentage of oxidative carbon (C–O, C=O) is 23.1%, confirming the existence of a mildly oxidative carbon overlayer.[52] The O 1s spectra are decomposed using five different components: 533.23 eV for C–O, 533.88 eV for O–C=O, 532.25 eV for –OH, 531.41 eV for C=O, and 530.87 eV for Sn–O–Ta (Fig. 3(f)).

The resistivity measurements were conducted on the $Sn_{1-x}Ta_xO_2$ nanowall films to learn about the electrical conductivity. Fig. S4† shows the specific resistivity as a function of doping level for SnO_2 nanowall films. The specific resistivity of the SnO_2 nanowall film decreases significantly after the doping of Ta, and achieves the lowest level at the doping amount of 7.5 mol%. The high conductivity of the Ta-doped nanowall film guarantees its excellent performance for use as a catalyst support.

Electrochemical behavior of the $Sn_{1-x}Ta_xO_2$/C sample

As one example for the applications of $Sn_{1-x}Ta_xO_2$/C, its electrochemical properties were assessed in fully flexible DSSC devices. Fig. S5† shows the configuration of fully flexible DSSCs in this study. Fig. 4(a) demonstrates the photocurrent–voltage (j–V) curves of fully flexible DSSCs, and the photovoltaic parameters are displayed in Table 2. As shown in Table 2, the short-circuit photocurrent density (j_{sc}), open-circuit voltage (V_{oc}), and fill factor of flexible DSSCs based on $Sn_{0.925}Ta_{0.075}O_2$/C CE are 16.53 mA cm^{-2}, 705 mV and 0.72, respectively, yielding an overall energy-conversion efficiency of 8.38%, which is remarkably comparable to that of fully flexible DSSCs with Pt CE (8.46%). The fully flexible DSSCs based on bare SnO_2 as the counter electrode showed a short circuit current density (j_{sc}) of 8.13 mA cm^{-2}, an open circuit voltage (V_{oc}) of 435 mV, a fill factor (FF) of 0.40, and a power conversion efficiency (η) of 1.40%. The lower values of photovoltaic parameters are

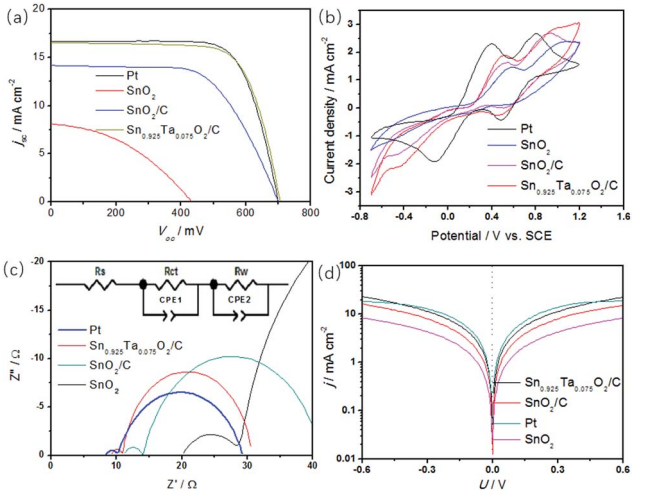

Fig. 4 (a) Current density–voltage (j–V) curves of fully flexible DSSCs. To get a clear picture, other j–V curves based on the $Sn_{1-x}Ta_xO_2$/C hybrid structure are shown in Fig. S6.† (b) Cyclic voltammograms of different counter electrodes at a scan rate of 50 mV s^{-1}. Electrolyte: 0.1 M $LiClO_4$, 10 mM LiI and 1 mM I_2 in acetonitrile solution. Reference electrode: saturated calomel electrode. (c) Nyquist plots of the TiO_2/PEN photoanode-based fully flexible DSSCs employing four different CEs, obtained in open circuit conditions. The inset is the equivalent circuit of fully flexible DSSCs. (d) Tafel curves of the symmetrical cells fabricated with two identical Pt, SnO_2, SnO_2/C, and $Sn_{0.925}Ta_{0.075}O_2$/C CEs.

Table 2 j–V characteristics of fully flexible DSSCs employing various CEs[a]

	j_{sc} (mA cm^{-2})	V_{oc} (mV)	η (%)	FF
Pt	16.67	695	8.46	0.73
SnO_2	8.13	435	1.40	0.40
SnO_2/C	14.17	700	6.15	0.62
$Sn_{0.975}Ta_{0.025}O_2$/C	15.79	700	7.49	0.68
$Sn_{0.95}Ta_{0.05}O_2$/C	16.06	705	7.95	0.70
$Sn_{0.925}Ta_{0.075}O_2$/C	16.53	705	8.38	0.72
$Sn_{0.9}Ta_{0.1}O_2$/C	16.07	700	7.92	0.70

[a] All data in the table are the mean values of ten samples, and the j–V data were obtained under AM 1.5 simulated sunlight (100 mW cm^{-2}). The photoactive area is 0.2 cm^2.

attributed to the high R_{ct} and R_s of SnO_2 electrodes as studied by EIS. Compared with the bare SnO_2 DSSCs, the SnO_2/C DSSCs yield a dramatically improved PCE of 6.15%, which is due to the high catalytic activity of surface coated carbon. After Ta doping in SnO_2/C, the photovoltaic performance is further enhanced. When 2.5 mol% Ta is doped into the electrode ($Sn_{0.975}Ta_{x0.025}O_2$/C), j_{sc} increases from 14.17 to 15.79 mA cm^{-2}. The optimal η reaches 8.38% at a Ta/Sn ratio of 7.5 mol% ($Sn_{0.925}Ta_{x0.075}O_2$/C). This can be partly attributed to the greatly improved electronic conductivity of SnO_2 after Ta doping. Despite the fact that V_{oc} only has a slight increase from 700 mV to 705 mV, η still obtains a certain degree of improvement owing to a substantial increase in the FF and j_{sc}. If the percent of Ta is up to 10 mol%, photoconversion efficiency begins to decline due to the decrease of FF and j_{sc}. The long-term stability of fully flexible DSSCs assembled with $Sn_{0.925}Ta_{0.075}O_2$/C electrodes was evaluated. As shown in Fig. S7,† the efficiency of fully flexible DSSCs remains almost constant for 100 hours. This result indicates that the $Sn_{0.925}Ta_{0.075}O_2$/C electrode based fully flexible DSSCs are a promising candidate for practical solar cells with good durability.

Cyclic voltammetry is a powerful tool to determine the catalytic activity of catalysts.[53,54] The electro-catalytic activity of different counter electrodes was first evaluated by cyclic voltammetry for the triiodide/iodide under the same conditions, and the results are shown in Fig. 4(b). Both curves exhibit two pairs of oxidation and reduction peaks. The left and right pairs are assigned to eqn (4) and (5), respectively. Apparently, the left cathodic peaks are the focus of our analysis because the CE is responsible for catalyzing the reduction of I_3^- to I^-.

$$I_3^- + 2e^- \leftrightarrow 3I^- \quad (4)$$

$$3I_2 + 2e^- \leftrightarrow 2I_3^- \quad (5)$$

The SnO_2 based electrode exhibited the lowest response current density, in accordance with its poor PCE. After carbon coating, the SnO_2/C electrode shows a greatly increased current density. Compared to the SnO_2/C electrode, the current density was further increased (by 53%) when the $Sn_{0.925}Ta_{0.075}O_2$/C electrodes were utilized as the working electrode, indicating that the triiodide reduction rate on the $Sn_{0.925}Ta_{0.075}O_2$/C electrode is the highest. Especially, the redox peaks of $Sn_{0.925}Ta_{0.075}O_2$/C at low potentials exhibited a current density higher than that for Pt, indicating a better catalytic activity.

To provide electrochemical insight into the electrochemical activity of SnO_2, SnO_2/C, $Sn_{0.925}Ta_{0.075}O_2$/C, and Pt, electrochemical impedance spectroscopy (EIS) was employed to investigate the charge transfer process in the DSSCs. The results are shown in the form of typical Nyquist plots, as illustrated in Fig. 4(c). The equivalent circuit model for fitting is described in the inset of Fig. 4(c) and the resultant parameters are summarized in Table 3, in which R_s is the series resistance and R_{ct} is the charge transfer resistance at the electrode/electrolyte interface. The R_s and R_{ct} values of SnO_2 are 20.2 Ω and 8.2 Ω, respectively. In contrast to SnO_2, smaller R_s and R_{ct} of the SnO_2/C can be observed, in which the R_s is mainly composed of the bulk resistance of SnO_2/C, Ti foil, contact resistance and so on. Note that when compared to SnO_2/C, the novel hybrid $Sn_{0.925}Ta_{0.075}O_2$/C nanostructure shows much lower R_s and R_{ct}, which is close to those of the Pt electrode, indicating much higher conductivity and catalytic activity. Therefore, it can be revealed that the catalytic activity for I_3^- reduction would be significantly enhanced with the $Sn_{0.925}Ta_{0.075}O_2$/C CE, which is in accordance with the CV results. To further characterize the properties of the counter electrodes, the electrical double-layer capacitance, which is related to the surface area, was obtained by fitting the Nyquist plots shown in Fig. 4(c). The chemical capacitances (C_m) of SnO_2/C and $Sn_{0.925}Ta_{0.075}O_2$/C are 2.10 and 2.36 mF, respectively, indicating a high surface area as compared to Pt which is advantageous for higher catalytic activity.

Tafel tests for Pt, SnO_2, SnO_2/C, and $Sn_{0.925}Ta_{0.075}O_2$/C CEs were performed to further confirm the catalytic activity. From the Tafel curves, we can obtain the exchange current density (j_0) and the limiting diffusion current density (j_{lim}), which are closely associated with the catalytic activity of the CEs. Fig. 4(d) shows the current density (j_0) as a function of voltage (U) at 25 °C for the oxidation/reduction of triiodide to iodide. As shown in Fig. 4(d), SnO_2 shows the smallest j_0, indicating poor catalytic activity, in good agreement with the EIS and CV results. In contrast, the slope of the $Sn_{0.925}Ta_{0.075}O_2$/C curve is slightly lower than that of Pt, indicating a roughly similar j_0 in terms of the following equation.

$$j_0 = RT/nFR_{ct} \quad (6)$$

where R is the gas constant, T is the temperature, F is the Faraday's constant and n is the number of electrons involved in

Table 3 Results of the impedance measurements[a]

samples	R_s	R_{ct} (Ω cm^{-2})	mF/cm^{-2}
Pt	7.2	2.0	0.14
SnO_2	20.2	8.2	1.66
SnO_2/C	11.5	3.6	2.10
$Sn_{0.925}Ta_{0.075}O_2$/C	9.0	2.1	2.36

[a] Measurement details for other $Sn_{1-x}Ta_xO_2$/C hybrid structures are shown in Table S1.

the electrochemical reduction of triiodide at the electrode. The j_{lim} of $Sn_{0.925}Ta_{0.075}O_2$/C is higher than that of Pt, SnO_2 and SnO_2/C, indicating that $Sn_{0.925}Ta_{0.075}O_2$/C has a higher diffusion coefficient after doping and consequently a higher diffusion velocity for the redox couple in the electrolyte. Based on this systematic evaluation of electrocatalytic activity, it is clear that $Sn_{0.925}Ta_{0.075}O_2$/C demonstrates superior catalytic activity for I_3^- reduction and results in competitive photovoltaic performance. $Sn_{0.925}Ta_{0.075}O_2$/C is expected to replace Pt as a potential CE catalyst in DSSCs.

Discussions about the high catalytic activity of $Sn_{1-x}Ta_xO_2$/C

First principles calculations are finally employed to understand the high catalytic activity of $Sn_{1-x}Ta_xO_2$/C. The effect of Sn atoms partially substituted by the Ta atoms was first studied by calculating the density of states (DOS) for bulk $Sn_{1-x}Ta_xO_2$. The calculated band gap of SnO_2 is 2.13 eV, which is larger than that of the calculation result of 1.7 eV using the FP-LAPW method[55] but is lower than that of the experimental value of 3.597 eV.[56] It is well known that the GGA method underestimates the band gap, especially for the system with strong correlations or weak Coulomb screening. The band gap can be corrected to be 3.43 eV by using the HSE hybrid functional calculations (*RSC Adv.*, 2015, **5**, 93765–93772), which is very close to the experimental value. However, both GGA and HSE results predict the same trend of variation for the band gap and the Fermi level shift under different doping concentrations. To keep the same method for the later calculations of SnO_2/C systems, we all use the GGA method in this work due to the large cost to calculate the interface model by the HSE method.

We calculated the formation energies for the doping site of substituting a Sn atom and an interstitial site, respectively, and found that compared with Ta doping at an interstitial, Ta substituting a Sn atom will be energetically favorable. For each x value, we have considered at least four substitution structures and found out there is a little difference among them. Fig. S2† shows the doping model and the DOS for $Sn_{1-x}Ta_xO_2$ with different substitution degrees. Our calculations clearly revealed a gradual shift of the Fermi level toward the conduction band with Sn substituted by Ta. The Fermi level shift reaches up to 2.25 eV with the Ta doping content increasing from $x = 0.0$ to $x = 0.075$, and then nearly saturates (Fig. S2(c)†). By contrast, the band gap is nearly unchanged when the Sn atoms are substituted by the Ta atoms. The Fermi level shifts upward to the conduction band showing that there is an n-type doping effect when Sn is substituted by Ta for SnO_2. From Fig. S2(b),† we can see that the Fermi level first locates at the valence band maximum for SnO_2 and then locates very close to the conduction band minimum for $Sn_{0.975}Ta_{0.025}O_2$, indicating that substitution of Sn sites by Ta introduces a shallow donor level. This is attributed to the fact that Ta atoms (5^+) possess one more valence electron than Sn atoms (4^+), which also accounts for the n-type doping effect. The n-type doping effect will increase the electron concentration and contribute to the electrical conductance, as suggested by our experimental results when Sn is substituted by Ta at a degree of $x = 0.025$, 0.05, 0.075, and 0.1. In Fig. S4,† the electrical conductance first increased with the Ta content increasing from $x = 0$ to $x = 0.075$, and then decreased with the Ta content increasing from $x = 0.075$ to $x = 0.1$. When the Ta doping is under the level of $x = 0.075$, the increased electrical conductance is mainly attributed to the increased intrinsic doping effect caused by the substitution of Sn by Ta. The higher levels of Ta doping not improving the electrical conductivity can be attributed to three reasons: first, the Fermi level shift nearly saturates when the Ta doping level exceeds $x = 0.075$; second, the increasing Ta contents could introduce more impurity scattering centers, which will impede the electron transport and decrease the carrier mobility; third, it is possible that with the increasing Ta/Sn ratio, some of the Sn vacancies were formed to balance the valences of the sample's constituent elements, which will hinder the electron concentration from increasing. The increasing electronic conductance of $Sn_{1-x}Ta_xO_2$ will benefit the electron transport from the $Sn_{0.925}Ta_{0.075}O_2$ support to carbon layers.

To further investigate the properties of $Sn_{1-x}Ta_xO_2$/C, the slab is built as shown in Fig. 5. We consider two high-symmetry initial configurations (Fig. 5(a) and (b)) of graphene on $Sn_{1-x}Ta_xO_2$ (110) surfaces. In general, a high-symmetry configuration is more stable than a low-symmetry one and often selected as the initial configuration. After optimization, the energy of the second configuration is lower, so we choose it for subsequent calculations. We calculate the SnO_2/C and $Sn_{0.9275}Ta_{0.0625}O_2$/C systems to compare the effect of doping Ta and qualitatively analyze the effect using the result of doping Ta atoms to obtain the charge density difference. The equilibrium interfacial distance d_{O-C} is defined as the difference between the average z-coordinates (vertical to the interface) of the C atoms and the topmost O atoms (Fig. 5(d)). The d_{O-C} of SnO_2/C and $Sn_{0.9275}Ta_{0.0625}O_2$/C systems is 2.96 Å and 3.18 Å, respectively,

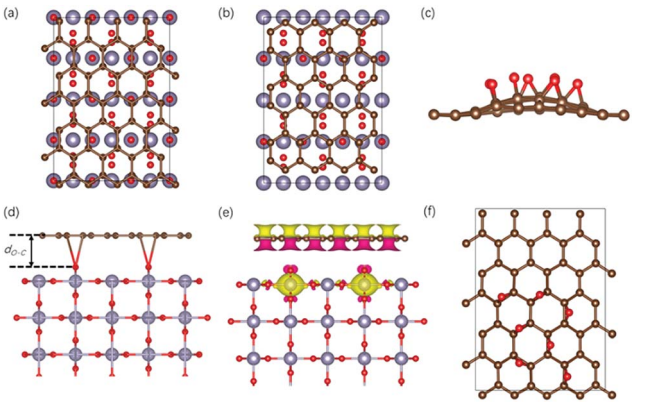

Fig. 5 (a) Top view of the first configuration of $Sn_{1-x}Ta_xO_2$/C. (b) Top view of the second configuration of $Sn_{1-x}Ta_xO_2$/C. (c) Side view of the most stable adsorption configuration of seven oxygen atoms on graphene. (d) Side view of graphene on the SnO_2 (110) surface. (e) The charge density difference between SnO_2/C and $Sn_{0.9275}Ta_{0.0625}O_2$/C. The yellow areas indicate the areas with more electrons, and the red areas indicate the area with less electrons comparing the charge density before and after doping Ta atoms. (f) Top view of the most stable adsorption configuration of seven oxygen atoms on graphene. Grey balls: Sn; green balls: Ta; red balls: O; brown balls: C.

indicating that graphene is physically adsorbed on SnO_2 and $Sn_{0.9275}Ta_{0.0625}O_2$. The difference of charge density between SnO_2/C and $Sn_{0.9275}Ta_{0.0625}O_2$/C systems is shown in Fig. 5(e). It can be seen that after doping Ta atoms, the electron density of the upper surface of graphene is increased obviously, indicating that a big improvement in catalysis has been introduced by $Sn_{0.9275}Ta_{0.0625}O_2$/C than SnO_2/C.

The work functions of graphene, graphene oxide, $Sn_{0.9275}Ta_{0.0625}O_2$, and SnO_2 are calculated next, which are shown in Fig. 6. The work function of SnO_2 decreases by 0.70 eV after doping Ta atoms, indicating that Ta doping can decrease the work function of SnO_2. It is reasonable to assume that graphene is oxidized, because the C–O peak is observed in XPS spectra. We adopt the structure of graphene oxide from the result given by Li *et al.*[57] $C_{48}O_1$, $C_{48}O_2$, $C_{48}O_3$, $C_{48}O_5$ and $C_{48}O_7$ are considered, and the optimized structures are consistent with Li *et al.*'s work.[57] Obviously, the higher oxidation degree of graphene leads to higher work function. As shown in Fig. 6(a), we use a fitted linear model based on the work function of graphene oxide ($C_{48}O_1$, $C_{48}O_2$, $C_{48}O_3$, $C_{48}O_5$ and $C_{48}O_7$). The slope is 0.13, the intercept is 4.75, and the $R^2 = 0.983$. The work function of $C_{48}O_{10.5}$ (O/C = 21.8%) will exceed that of $Sn_{0.0975}Ta_{0.0625}O_2$ according to the fitted model. According to the experimental results, the ratio of O to C is larger than 20% (XPS data). So when the work function of graphene oxide exceeds that of $Sn_{0.0975}Ta_{0.0625}O_2$, electrons will transfer from $Sn_{0.0975}Ta_{0.0625}O_2$ to graphene oxide. Pushing more electrons from $Sn_{0.0975}Ta_{0.0625}O_2$ to carbon layers will significantly improve the catalytic activity. According to the charge density difference and work function results, substitution of Sn atoms by Ta atoms will markedly reduce the work function of SnO_2 which makes the electron transfer from SnO_2 to graphene oxide easy. Increasing the number of electrons on carbon layers leads to a great improvement in catalytic activity.

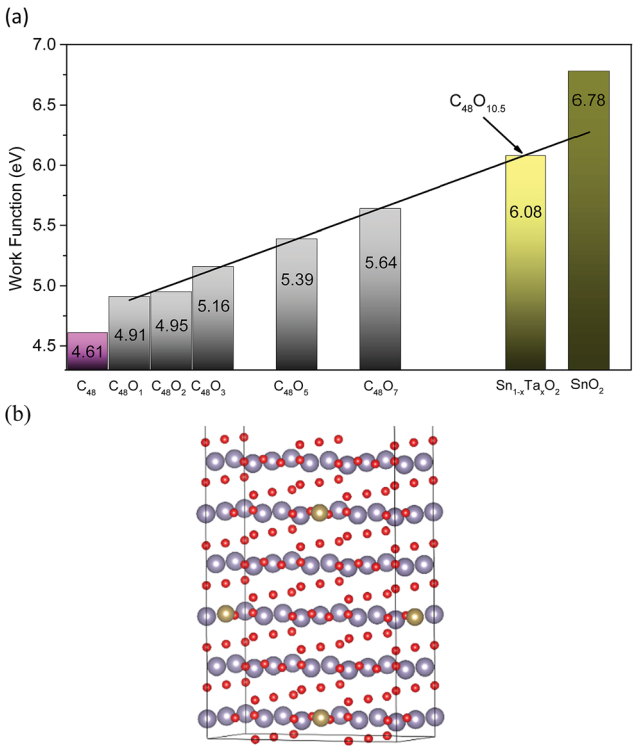

Fig. 6 (a) The work function of graphene (C_{48}), graphene oxide ($C_{48}O_1$, $C_{48}O_2$, $C_{48}O_3$, $C_{48}O_5$ and $C_{48}O_7$), $Sn_{1-x}Ta_xO_2$/C ($x = 0.0625$, $Sn_{0.9275}Ta_{0.0625}O_2$) and SnO_2. The line is the fitted linear model based on the work function of graphene oxide. The slope is 0.13, the intercept is 4.75, and the $R^2 = 0.983$. The work function of $C_{48}O_{10.5}$ will exceed that of $Sn_{0.9275}Ta_{0.0625}O_2$ according to the fitted model. (b) Structure of the slab of $Sn_{0.9275}Ta_{0.0625}O_2$.

Conclusion

Herein, a hybrid $Sn_{1-x}Ta_xO_2$/C nanostructure was fabricated which exhibits good stability and electrocatalytic activity for electrochemical reduction. As one example, flexible DSSCs based on this new type of counter electrode showed a comparable performance to those based on a Pt counter electrode. The high catalytic activity can be mainly attributed to the fact that the Ta doped SnO_2 not only acts as a well conductive support for the close coated graphene-like carbon layers but also pushes electrons to the carbon electrocatalyst to enhance its catalytic activity. The as-developed hybrid $Sn_{1-x}Ta_xO_2$/C nanostructure is a highly promising material for use in flexible energy storage and conversion devices, and the design strategy described here could easily be extended to other transparent conductive oxides (*e.g.*, doped-In_2O_3 and doped-ZnO) and catalytic materials.

Acknowledgements

This work was financially supported by the Shenzhen Science and Technology Research Grant (No. JCYJ20120614150338154) and National Natural Science Foundation of China (51602010; 61604058).

Notes and references

1 M. P. Kumar, M. M. Raju, A. Arunchander, S. Selvaraj, G. Kalita, T. N. Narayanan, A. K. Sahu and D. K. Pattanayak, *J. Electrochem. Soc.*, 2016, **163**, F848–F855.
2 T. Palaniselvam, V. Kashyap, S. N. Bhange, J. B. Baek and S. Kurungot, *Adv. Funct. Mater.*, 2016, **26**, 2150–2162.
3 S. J. You, X. B. Gong, W. Wang, D. P. Qi, X. H. Wang, X. D. Chen and N. Q. Ren, *Adv. Energy Mater.*, 2016, **6**, 1501497.
4 M. R. Nellist, F. A. L. Laskowski, F. D. Lin, T. J. Mills and S. W. Boettcher, *Acc. Chem. Res.*, 2016, **49**, 733–740.
5 M. Ledendecker, S. K. Calderon, C. Papp, H. P. Steinruck, M. Antonietti and M. Shalom, *Angew. Chem., Int. Ed.*, 2015, **54**, 12361–12365.
6 M. Gong, W. Zhou, M. J. Kenney, R. Kapusta, S. Cowley, Y. P. Wu, B. A. Lu, M. C. Lin, D. Y. Wang, J. Yang, B. J. Hwang and H. J. Dai, *Angew. Chem., Int. Ed.*, 2015, **54**, 11989–11993.
7 J. Briscoe and S. Dunn, *Adv. Mater.*, 2016, **28**, 3802–3813.
8 Y. D. Xing, X. J. Zheng, Y. H. Wu, M. R. Li, W. H. Zhang and C. Li, *Chem. Commun.*, 2015, **51**, 8146–8149.

9 C. Y. Zhang, Y. H. Xie, J. H. Ma, J. Hu and C. C. Zhang, *Chem. Commun.*, 2015, **51**, 17459–17462.
10 X. T. Meng, C. Yu, X. D. Song, Y. Liu, S. X. Liang, Z. Q. Liu, C. Hao and J. S. Qiu, *Adv. Energy Mater.*, 2015, **5**, 9.
11 M. Batmunkh, M. J. Biggs and J. G. Shapter, *Adv. Sci.*, 2015, **2**, 16.
12 M. Wu, X. Lin, Y. Wang, L. Wang, W. Guo, D. Qi, X. Peng, A. Hagfeldt, M. Grätzel and T. Ma, *J. Am. Chem. Soc.*, 2012, **134**, 3419–3428.
13 Z. M. He, J. Liu, S. Y. Khoo and T. T. Y. Tan, *Chemsuschem*, 2016, **9**, 172–176.
14 K. Aitola, M. Borghei, A. Kaskela, E. Kemppainen, A. G. Nasibulin, E. I. Kauppinen, P. D. Lund, V. Ruiz and J. Halme, *J. Electroanal. Chem.*, 2012, **683**, 70–74.
15 S. Yun, A. Hagfeldt and T. Ma, *Adv. Mater.*, 2014, **26**, 6210–6237.
16 M. Wu and T. Ma, *J. Phys. Chem. C*, 2014, **118**, 16727–16742.
17 W. J. Lee, E. Ramasamy, D. Y. Lee and J. S. Song, *Sol. Energy Mater. Sol. Cells*, 2008, **92**, 814–818.
18 W. W. Sun, X. H. Sun, T. Peng, Y. M. Liu, H. W. Zhu, S. S. Guo and X. Z. Zhao, *J. Power Sources*, 2012, **201**, 402–407.
19 A. Kay and M. Grätzel, *Sol. Energy Mater. Sol. Cells*, 1996, **44**, 99–117.
20 M. Wu, X. Lin, T. Wang, J. Qiu and T. Ma, *Energy Environ. Sci.*, 2011, **4**, 2308–2315.
21 A. Hauch and A. Georg, *Electrochim. Acta*, 2001, **46**, 3457–3466.
22 Y. Hou, D. Wang, X. H. Yang, W. Q. Fang, B. Zhang, H. F. Wang, G. Z. Lu, P. Hu, H. J. Zhao and H. G. Yang, *Nat. Commun.*, 2013, **4**, 1583.
23 L. D. Wang, B. Wei, P. Dong, Q. H. Miao, Z. Liu, F. B. Xu, J. J. Wu, J. Lou, R. Vajtai and W. D. Fei, *Mater. Design*, 2016, **92**, 462–470.
24 X. P. Wang, Q. W. Tang, B. L. He, R. Lia and L. M. Yu, *Chem. Commun.*, 2015, **51**, 491–494.
25 J. J. Lin, Y. Peng, A. R. Pascoe, F. Z. Huang, Y. B. Cheng, Y. U. Heo, A. Nattestad, W. Seung, S. K. Kim, H. J. Yoon, S. W. Kim, Y. Yamauchi, S. X. Dou and J. H. Kim, *J. Mater. Chem. A*, 2015, **3**, 4679–4686.
26 K. Yoo, J. Y. Kim, J. A. Lee, J. S. Kim, D. K. Lee, K. Kim, J. Y. Kim, B. Kim, H. Kim, W. M. Kim, J. H. Kim and M. J. Ko, *ACS Nano*, 2015, **9**, 3760–3771.
27 L. X. Song, Y. L. Guan, P. F. Du, Y. F. Yang, F. Ko and J. Xiong, *Sol. Energy Mater. Sol. Cells*, 2016, **147**, 134–143.
28 W. X. Song, H. Wang, G. C. Liu, M. Peng and D. C. Zou, *Nano Energy*, 2016, **19**, 1–7.
29 T. Chen and L. M. Dai, *Angew. Chem., Int. Ed.*, 2015, **54**, 14947–14950.
30 G. C. Liu, X. Gao, H. Wang, A. Y. Kim, Z. X. Zhao, J. K. Lee and D. C. Zou, *J. Mater. Chem. A*, 2016, **4**, 5925–5931.
31 X. J. Zhang, W. X. Guo and C. F. Pan, *J. Mater. Chem. A*, 2016, **4**, 6569–6576.
32 J. Liang, G. M. Zhang, W. T. Sun and P. Dong, *Nano Energy*, 2015, **12**, 501–509.
33 L. Y. Lin, M. H. Yeh, K. W. Tsai, C. Y. Chen, C. G. Wu and K. C. Ho, *Electrochem. Commun.*, 2013, **37**, 71–75.
34 V. D. Dao, C. Q. Tran, S. H. Ko and H. S. Choi, *J. Mater. Chem. A*, 2013, **1**, 4436–4443.
35 P. Dong, Y. Zhu, J. Zhang, F. Hao, J. J. Wu, S. D. Lei, H. Lin, R. H. Hauge, J. M. Tour and J. Lou, *J. Mater. Chem. A*, 2014, **2**, 20902–20907.
36 F. Z. Huang, D. H. Chen, Y. Chen, R. A. Caruso and Y. B. Cheng, *J. Mater. Chem. C*, 2014, **2**, 1284–1289.
37 K. M. Lee, L. C. Lin, V. Suryanarayanan and C. G. Wu, *J. Power Sources*, 2014, **269**, 789–794.
38 P. Bonhôte, A.-P. Dias, N. Papageorgiou, K. Kalyanasundaram and M. Grätzel, *Inorg. Chem.*, 1996, **35**, 1168–1178.
39 N.-Q. Fu, Y.-Y. Fang, Y.-D. Duan, X.-W. Zhou, X.-R. Xiao and Y. Lin, *ACS Nano*, 2012, **6**, 9596–9605.
40 N.-Q. Fu, Y.-D. Duan, Y.-Y. Fang, X.-W. Zhou, X.-R. Xiao and Y. Lin, *Electrochem. Commun.*, 2013, **34**, 254–257.
41 H. J. Monkhorst and J. D. Pack, *Phys. Rev. B*, 1976, **13**, 5188–5192.
42 P. E. Blöchl, *Phys. Rev. B: Condens. Matter Mater. Phys.*, 1994, **50**, 17953–17979.
43 G. Kresse and D. Joubert, *Phys. Rev. B: Condens. Matter Mater. Phys.*, 1999, **59**, 1758–1775.
44 G. Kresse and J. Furthmuller, *Comput. Mater. Sci.*, 1996, **6**, 15–50.
45 G. Kresse and J. Furthmuller, *Phys. Rev. B: Condens. Matter Mater. Phys.*, 1996, **54**, 11169–11186.
46 J. P. Perdew, K. Burke and M. Ernzerhof, *Phys. Rev. Lett.*, 1996, **77**, 3865–3868.
47 Y. Wang, I. Djerdj, B. Smarsly and M. Antonietti, *Chem. Mater.*, 2009, **21**, 3202–3209.
48 Y.-S. Lin, J.-G. Duh and M.-H. Hung, *J. Phys. Chem. C*, 2010, **114**, 13136–13141.
49 O. Akhavan, *ACS Nano*, 2010, **4**, 4174–4180.
50 C. Zhang, X. Peng, Z. Guo, C. Cai, Z. Chen, D. Wexler, S. Li and H. Liu, *Carbon*, 2012, **50**, 1897–1903.
51 Z. Zhang, R. Dua, L. Zhang, H. Zhu, H. Zhang and P. Wang, *ACS Nano*, 2013, **7**, 1709–1717.
52 Z. Shen, Y. Hu, Y. L. Chen, R. Z. Chen, X. He, X. W. Zhang, H. F. Shao and Y. Zhang, *Electrochim. Acta*, 2016, **188**, 661–670.
53 J. D. Roy-Mayhew, D. J. Bozym, C. Punckt and I. A. Aksay, *ACS Nano*, 2010, **4**, 6203–6211.
54 K. Jost, C. R. Perez, J. K. McDonough, V. Presser, M. Heon, G. Dion and Y. Gogotsi, *Energy Environ. Sci.*, 2011, **4**, 5060–5067.
55 L. A. Errico, *Phys. Rev. B: Condens. Matter Mater. Phys.*, 2007, **389**, 140–144.
56 V. T. Agekyan, *Phys. Status Solidi A*, 1977, **43**, 11–42.
57 X.-B. Li, P. Guo, D. Wang, Y. Zhang and L.-M. Liu, *J. Chem. Phys.*, 2014, **141**, 224703.